Factors responsible for crystal-chemical variations in the solid solutions from illite to aluminoceladonite and from glauconite to celadonite

Victor A. Drits,[1] Bella B. Zviagina,[1] Douglas K. McCarty,[2,*] and Alfred L. Salyn[1]

[1]Geological Institute of the Russian Academy of Science, Pyzhevsky per. 7, 119017 Moscow, Russia
[2]Chevron ETC, 3901 Briarpark, Houston, Texas 77063, U.S.A.

Abstract

Several finely dispersed low-temperature dioctahedral micas and micaceous minerals that form solid solutions from (Mg,Fe)-free illite to aluminoceladonite via Mg-rich illite, and from Fe^{3+}-rich glauconite to celadonite have been studied by X-ray diffraction and chemical analysis. The samples have 1*M* and 1*Md* structures. The transitions from illite to aluminoceladonite and from glauconite to celadonite are accompanied by a consistent decrease in the mica structural-unit thickness (2:1 layer + interlayer) or $c\sin\beta$. In the first sample series $c\sin\beta$ decreases from 10.024 to 9.898 Å, and in the second from 10.002 to 9.961 Å. To reveal the basic factors responsible for these regularities, structural modeling was carried out to deduce atomic coordinates for 1*M* dioctahedral mica based on the unit-cell parameters and cation composition. For each sample series, the relationships among $c\sin\beta$, maximum and mean thicknesses of octahedral and tetrahedral sheets and of the 2:1 layer, interlayer distance, and variations of the tetrahedral rotation angle, α, and the degree of basal surface corrugation, ΔZ, have been analyzed in detail.

The transitions from illite to aluminoceladonite and from glauconite to celadonite are accompanied by a slight increase in the mean thickness of the 2:1 layers and a steady decrease in the α angles, whereas the interlayer distance becomes smaller. These results are consistent with the generally accepted model where tetrahedral rotation is the main factor for the interlayer contraction in muscovite-phengite structures: the smaller the rotation angle (α) the larger the ditrigonal ring of the tetrahedral sheet and the interlayer pseudo-hexagonal cavity, allowing the interlayer cation to sink and thus shorten the *c* parameter.

A new insight into the interpretation of the contraction of the mica layer thickness in dioctahedral micas has been achieved with the discovery that micas with the same or close mean interlayer distance, on one hand, have the same or nearly the same substitution of Al for Si; and on the other hand, they may have significantly different parameters of the interlayer structure, such as tetrahedral rotation, basal surface corrugation, ΔZ, and minimum and maximum interlayer distance. These results show that in dioctahedral 1*M* micas, the mean interlayer distance is determined by the amount of tetrahedral Al because the higher the Al for Si substitution, the stronger the repulsion between the basal O atoms and the larger the interlayer distance and $c\sin\beta$ parameter.

Keywords: Illite, aluminoceladonite, glauconite, celadonite, modeling, structural features, XRD

Introduction

Potassium dioctahedral micas are rock-forming minerals that occur in various geologic environments and in sedimentary, metamorphic, and igneous rocks. The mica structure consists of 2:1 layers separated by interlayer K cations. A 2:1 layer consists of two tetrahedral sheets linked through an octahedral sheet. The octahedral sheet contains three symmetrically independent sites that differ in the arrangement of OH groups and oxygen anions coordinating octahedral cations. In the *trans*-octahedra, the OH groups occupy opposite apices, whereas in the *cis*-octahedra, the OH groups form a shared edge. Normally, the structure of dioctahedral micas is described in terms of 1*M*, 2*M*₁, 2*M*₂, and 3*T* polytypes differing in mutual arrangement of the adjacent layers (Bailey 1984). Structure studies of 2*M*₁, 2*M*₂, and 3*T* di-octahedral micas have shown that octahedral cations in their 2:1 layers typically occupy only *cis* sites (Bailey 1984; Brigatti and Guggenheim 2002). In 1*M* dioctahedral micas, the distribution of octahedral cations over symmetrically independent sites is more variable. In particular, 1*M* structures may consist of either *trans*-vacant (*tv*) or *cis*-vacant (*cv*) 2:1 layers, or of interstratified layer types (see Drits et al. 2006 for review).

Diverse isomorphous cation substitutions in both octahedral and tetrahedral sheets of the 2:1 layers are a characteristic feature of dioctahedral micas. High-temperature potassium dioctahedral micas form a solid solution between muscovite $KAl_2(Si_3Al)O_{10}(OH)_2$ and phengite, $KAl_{1.5}Mg_{0.5}(Si_{3.5}Al_{0.5})O_{10}(OH)_2$ (Brigatti and Guggenheim 2002; Ferraris and Ivaldi 2002). The 2*M*₁ and 3*T* micas with cation compositions intermediate between phengite and aluminoceladonite, $KAlMgSi_4O_{10}(OH)_2$, have not been found among natural dioctahedral micas. However, Smyth et al. (2000) synthesized a dioctahedral Al,Mg-bearing sample consisting of 2*M*₁ and 3*T* polytypes with 3.8 Si per half-formula unit (phfu). The synthesis was carried out at 900 °C and 11 GPa.

* E-mail: dmccarty@chevron.com

In contrast to high-temperature dioctahedral micas, low-temperature potassium dioctahedral micas and micaceous minerals normally occur as 1*M* and 1*Md* polytypes and are represented by illite, aluminoceladonite, celadonite, ferroceladonite, ferroaluminoceladonite, and glauconite (Środoń and Eberl 1984; Drits and Kossovskaya 1991; Li et al. 1997; Rieder et al. 1998; Brigatti and Guggenheim 2002). Moreover, isomorphous cation substitutions in these minerals are more diverse than in white micas (Drits et al. 2006).

In a single-crystal structure refinement, Güven (1971) showed that the *c* parameter and the tetrahedral rotation angle α are smaller in 2*M*$_1$ phengite than in 2*M*$_1$ muscovite. Based on the results of Güven (1971) and on the simulation of aluminoceladonite and celadonite structural features, Sokolova et al. (1976) showed that the thickness of the mica structural unit (*c*sinβ/*n* where *n* is the number of 2:1 layers in a unit cell) decreases from 9.973 Å for 2*M*$_1$ muscovite to 9.923 Å for 2*M*$_1$ phengite and to 9.885 Å for 1*M* aluminoceladonite because of a significant decrease in the interlayer distance. The minor decrease in the tetrahedral sheet thickness is almost compensated by the increase in the octahedral sheet thickness leading to a constant 2:1 layer thickness for these minerals.

Further investigations showed that in natural and synthetic potassium dioctahedral 2*M*$_1$ and 3*T* micas, which belong to the solid-solution muscovite-aluminoceladonite, the *c* parameter decreases over the total composition range (Massonne and Schreyer 1986, 1989; Guidotti et al. 1992; Schmidt et al. 2001; Ivaldi et al. 2001). It was concluded that the smaller the tetrahedral rotation angle, the larger are the ditrigonal rings of the tetrahedral sheets across the interlayers, where the interlayer cation can sink, and thus the shorter is the *c*sinβ/*n* value (Ferraris and Ivaldi 2002).

In contrast to high-temperature dioctahedral micas, the relationship between cation composition and thickness of the mica structural unit, *c*sinβ, have not been studied properly for low-temperature 1*M* illite, 1*M* celadonite, 1*M* aluminoceladonite, and 1*M* glauconite despite the wide range of isomorphous cation substitutions. Structure studies of these minerals are problematic as they are finely dispersed and often have low structural order. In addition, the *c*sinβ value of the low-temperature illite samples has been assumed to be equal to 9.98 Å, independent of their cation composition and conditions of formation (Środoń 1999; Środoń et al. 1992). The purposes of this study are (1) to demonstrate that the relationships found for high-temperature dioctahedral micas are valid for the illite-aluminoceladonite

series; (2) to consider structural and crystal-chemical features of the members in illite-Mg-rich illite-aluminoceladonite, and glauconite-celadonite groups; and, based on the comparison of these features, (3) to provide new insight into the factors controlling the contraction of the mica layer. To solve these problems the structural features for each particular member of the two groups were simulated with a modified version of the algorithm of Smoliar-Zviagina (1993).

EXPERIMENTAL METHODS

X-ray diffraction

Random powder samples were obtained from the <1.0 and <2.0 μm size fractions of selected samples, which were loaded in 0.8 mm capillaries after spray drying. High-resolution synchrotron powder diffraction data were collected on the 11-BM beamline at the Advanced Photon Source (APS), Argonne National Laboratory using an average wavelength of 0.414193 Å, with data points collected every 0.001 °2θ and a scan speed of 0.01°/s. A mixture of NIST standard reference materials, Si (SRM 640c) and Al$_2$O$_3$ (SRM 676) was used to calibrate the instrument. Corrections were applied for detector sensitivity, 2θ offset, small differences in wavelength between detectors, and the source intensity (Wang et al. 2008; Lee et al. 2008).

Random powder XRD patterns of the other portion of samples were collected with a θ-θ Thermo Xtra diffractometer with a 250 mm goniometer radius equipped with a solid state Si detector using side-loading sample mounts with a 10 wt% internal standard of the NIST SRM 640c Si powder mixed in with the sample to calibrate 2θ offset. Scans were made from 5 to 65 °2θ, with a 0.02° step increment, and a count time of 10 s or more per step using Cu*K*α radiation transmitted through a 1.00 mm divergence and 1.80 mm antiscatter slit. Detector slits were 2.00 and 0.3 mm.

Oriented aggregates were made by evaporation onto glass slides to provide a sample ~5 cm long with at least 10 mg clay per cm² (Moore and Reynolds 1997). Scans were collected using the same diffraction system in the air-dried (AD) state and in a nitrogen atmosphere after the oriented specimen was heated at 250° for 1 h. The scans were made from 2 to 52 °2θ with a 0.02 °2θ step increment and counting rate of 4 s per step or longer.

Samples

The studied samples are represented by illite, aluminoceladonite, celadonite, and glauconite, which form two solid solutions: (1) from (Mg, Fe)-free illite to aluminoceladonite via Mg-rich illite, and (2) from Fe-rich glauconite to celadonite. The samples have 1*M* or 1*Md* structures (see next section for details). Table 1 contains the mineral identifications, locations, expandability, and the references to publications containing mineralogical characterizations of the samples.

Determination of the unit-cell parameters

Analysis of the experimental powder XRD patterns shows that the samples are monomineralic dioctahedral 1*M* and 1*Md* micas and micaceous minerals. The determination and refinement of the unit-cell parameters of the mica structures were carried out using experimental *d*(*hkl*) values. The unit-cell parameters of five

TABLE 1. Sample description

Sample name	Mineral species	Location, reference, and cited expandable layer content
RM30	illite Mg-poor	Silver caldera, San Juan Mountains, Colorado; Eberl et al. (1987), 6–9%
M422	illite Mg-poor	Belgorod, Low Amur, Russia; Slonimskaya et al. (1978); Drits and McCarty (2007), 10%
10564	illite Mg-poor	Athabasca basement; Saskatchewan, Canada; Drits et al. (1993a)
Silver Hill	illite Mg-bearing	CMS, IMT-1 standard; Środoń and Eberl (1984), 1–2%
KJMC3	illite Mg-rich	Ordovician K-bentonite, Vermont; Ryan et al. (2007), 5–10%
Zempleni	Illite-smectite	Füzerradvany, Hungary; Viczian (1997); Środoń et al. (1992), ~15%
60	globular illite Mg-rich	South Urals, Russia; Ivanovskaya et al. (1989), 5–10%
602-1	alumino-celadonite	Twin Creek formation, Wyoming, This study
136	alumino-celadonite	Tushlay, Mongolia; Petrova and Amarjargal (1996)
69	celadonite	Krivoi Rog mining district, Russia; Lazarenko and Pavlishin (1976)
TAIH	celadonite Na-bearing	Taiheizan, Akita Prefecture, Japan; Kimbara and Shimoda (1973)
Z1	celadonite	Russia; Malkova (1956)
68-69	glauconite	Baltic region, Russia; Shutov et al. (1975); Drits et al. (1993b), 3–5%
PILT	glauconite	Ordovician sandstone, Latvia; Nikolaeva (1977); Drits et al. (1993b), 3–5%
BAB	glauconite	Leningrad region, Russia; Nikolaeva (1977); Drits et al. (1993b), 3–5%

samples (RM30, 602-1, 136, TAIH, Z1) recorded by synchrotron radiation (Fig. 1a) were refined by the least-squares technique using the Jade computer program (MDI, Inc.) (Table 2). To minimize the possible influence of expandable layers, the experimental $d(00l)$ were excluded from the refinement procedure. According to Kogure et al. (2008), the celadonite structures of samples TAIH and Z1 contain stacking faults related to layer rotation by 180° only. Such stacking faults shift hkl reflections with $h \neq 0$, whereas the positions of $0kl$ and $00l$ reflections are unaffected. However, the difference between the experimental and refined $d(hkl)$ values, with two or three exceptions, does not exceed the estimated standard deviation of the fits, which is 0.0041 °2θ for sample TAIH and 0.0022 °2θ for sample Z1.

Powder XRD patterns for samples 10564, M422, Zempleni, 60, Silver Hill, KJMC3, 68-69, BAB, and PILT, were recorded with a laboratory diffractometer and Cu radiation. Careful measurement of the positions of the reflections was made by mixing 10% of NIST SRM 640c Si powder with each sample (Fig. 1b). The powder XRD pattern of sample 10564 corresponds to cv 1*M* illite and the least-squares method was used to determine the unit-cell parameters. In agreement with the structural features of cv illite (Zviagina et al. 2007), the projection of the c axis onto the ab plane, as a fraction of the a axis ($c\cos\beta/a$), is significantly smaller in sample 10564 than in tv illite structures (Table 2). One of the remarkable features of the XRD pattern is that along with hkl reflections corresponding to cv 1*M* illite, it contains a set of weak but sharp reflections (Fig. 1b). The positions of these reflections correspond to those of tv 2*M*$_1$ illite. However, these reflections probably result from the regular interstratification of enantiomorphic cv 2:1 layers differing in the distribution of two symmetrically independent cis sites (Zviagina et al. 2007).

Samples M422 and Zempleni (Fig. 1b) contain stacking faults related to rotation of some layers by ±120° with respect to the layer orientation in the main 1*M* mica matrix (Drits et al. 1984). Nevertheless, the unit-cell parameters of the structures were refined with high precision (Table 2).

The structures of samples 60, 68-69, BAB, and PILT contain significant amounts of stacking faults associated with mutual rotation of some mica layers

by $n \cdot 60°$ ($n = 0, 1$–5) (Fig. 1b). According to Sakharov et al. (1990), in such structures, thin blocks with a periodic 1*M* structure are rotated by $n \cdot 60°$ with respect to each other with equal probability. The unit-cell parameters for these samples (Table 2) were determined by a combination of least-squares refinement and the trial-and-error technique to get the best possible agreement between measured and calculated $d(hkl)$.

The powder XRD patterns of samples Silver Hill and KJMC3 show that their structures contain a high amount of stacking faults related to random layer rotations by $n \cdot 60°$. Indeed, among 11l, 02l reflections only two wide intensity modulations in the regions of 11$\bar{2}$ and 112 reflections are observed (Fig. 1b). Therefore, the conventional way of determining the unit-cell parameters could not be applied to these samples (see below). Note that these samples, as well as others containing rotational stacking faults, are described in terms of the 1*Md*, rather than 1*M*, polytype.

One of the features of finely dispersed micaceous minerals is that they may contain expandable interlayers (Środoń and Eberl 1984). However, for samples 136, 602-1, 10564, TAIH, and Z1, the experimental and refined $d(00l)$ values coincide within the experimental errors, showing that the structures of these samples contain no or only a few expandable layers. The comparison of the experimental XRD patterns from non-heated and heated (at 250 °C) oriented specimens of the same sample recorded in air-dried and nitrogen atmospheres, respectively, show that samples PILT, Silver Hill, and KJMC3 contain about 5% of smectite interlayers, and the positions and profiles of basal reflections almost coincide (Fig. 2). The only noticeable difference is that the first low-angle reflections of the heated samples are slightly more narrow and intense than those of the non-heated samples (Fig. 2). Similar features of the basal reflections are observed from non-heated and heated partially oriented specimens for samples BAB, 60, 68-69, and RM30 (Fig. 2). This figure also shows that for samples BAB, 60, and 68-69, the positions and shapes of the non-basal reflections coincide for both heated and non-heated specimens. For sample RM30, the greater difference in the positions of basal reflections cor-
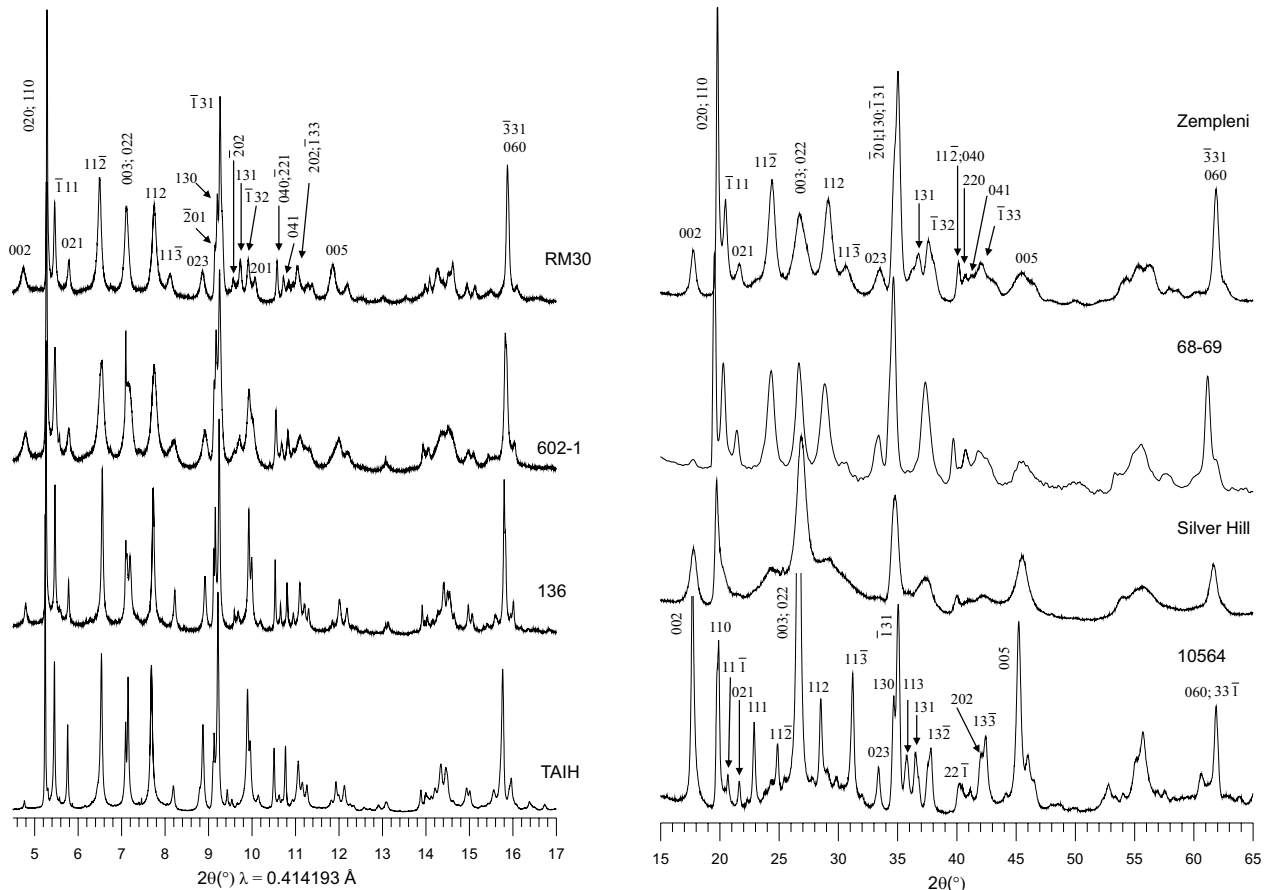

FIGURE 1. Powder XRD patterns for the selected samples: recorded using synchrotron radiation (left) and using conventional Cu radiation (right). The hkl indices are labeled for the tv 1*M* illite (RM30) and tv 1*M* illite fundamental particles (Zempline), and for cv 1*M* illite (10564).

TABLE 2. Unit-cell parameters* of the studied mineral species

Sample	Unit-cell parameter					
	a (Å)	*b* (Å)	*c* (Å)	β (°)	*c*sinβ (Å)	*c*cosβ/*a*
RM30	5.2021(4)	8.9797(6)	10.226(8)	101.57(1)	10.018	–0.394
M422	5.1994(1)	8.9815(7)	10.233(2)	101.60(2)	10.024	–0.396
10564	5.1973(9)	8.999(1)	10.147(2)	99.00(1)	10.022	–0.305
Silver Hill	5.208	9.020	10.166	101.5	9.963	–0.389
KJMC3	5.210	9.020	10.159	101.4	9.959	–0.385
60	5.235(1)	9.032(1)	10.140(5)	101.52(3)	9.936	–0.387
Zempleni	5.2042(2)	8.9852(3)	10.205(1)	101.49(1)	10.000	–0.391
602-1	5.2141(5)	9.0082(7)	10.108(1)	101.12(2)	9.918	–0.374
136	5.2227(3)	9.0195(3)	10.0767(8)	100.82(1)	9.898	–0.362
69	5.227(1)	9.052(1)	10.153(1)	100.53(2)	9.982	–0.355
TAIH	5.2313(7)	9.0511(9)	10.138(2)	100.71(2)	9.961	–0.360
Z1	5.2291(5)	9.051(1)	10.144(4)	100.59(2)	9.971	–0.356
68-69	5.246(4)	9.076(2)	10.184(2)	101.1(1)	9.993	–0.374
PILT	5.246(4)	9.066(2)	10.182(3)	101.2(2)	10.002	0.377
BAB	5.248(4)	9.074(2)	10.203(3)	101.4(3)	9.988	–0.384

* The space group for the mica structure is *C*2/*m* except for *cv* illite (sample 10564), which is *C*2.

responding to the heated and non-heated specimens is more pronounced mostly because of relatively high thickness of its coherent scattering domains (CSDs) (Fig. 2). In general, these results are in agreement with expandability of the studied samples determined by other authors (Table 1).

As mentioned, for the most disordered samples Silver Hill and KJMC3, the XRD patterns for the heated and non-heated specimens almost coincide. The average *d*(001) values for KJMC3 are 9.971 ± 0.007 Å for the air-dried and 9.959 ± 0.001 Å for the heated specimens. The *d*(001) value itself was excluded from the calculation of the average mica structural unit thickness because the 001 reflection is shifted to lower 2θ angles due to smaller CSD thickness (Drits and Tchoubar 1990). In addition, the rational series of basal reflections for the heated specimen

most probably originates from the fact that the mica structural unit thickness and the periodicity of completely dehydrated smectite along the *c** axis coincide, therefore for sample KJMC3 *d*(001) = 9.959(1) Å. The *b* and *a* parameters of the structure are assumed to be 6 × *d*(060) and *b*/√3, respectively. The trial-and-error procedure was used to determine the β angle for which the calculated and experimental *d*(22$\bar{1}$) and *d*($\bar{1}$31) values would almost coincide (Table 2). A similar approach was used to determine unit-cell parameters for the Silver Hill sample (Table 2).

The Zempleni illite has the I-S structure because the positions and profiles of the basal reflections in the XRD patterns of glycolated, air-dried, and heated oriented specimens of the sample differ substantially. However, the powder XRD pattern of the sample exhibits, despite the high expandability, high structural order in the stacking of illite layers (Fig. 1). In accordance with Reynolds (1992), the main contribution to the 3D diffraction effects can be assumed to be provided by illite fundamental particles that are separated from each other by smectite interlayers. The unit-cell parameters for sample 69 given in Table 2 were taken from the corresponding publication (Table 1).

Chemical analyses and structural formulae

The samples can be subdivided into two groups: those for which the chemical analyses and the corresponding structural formulae have been published in the literature, and the samples (602-1, 136, 10564, Silver Hill, KJCM3) for which chemical compositions were determined in this study by X-ray fluorescence spectrometry (Table 3). The structural formulae were calculated for $O_{10}(OH)_2$. The TAIH, Z1, 10564, 69, 602-1, and 136 samples are smectite free, while the others contain small amounts of smectite interlayers.

The dehydrated smectite layers were assumed to have a negative charge equal to 0.60 valence units (v.u.) because of their specific location as interfaces between illite fundamental particles. Their particular cation composition depends on the amount of tetrahedral Al cations (Al_t) in the average formula of the sample. If $Al_t \geq 0.5$, or $Al_t < 0.5$, then the smectite formula is $M^+_{0.60}(Si_{3.85}Al_{0.15})(R^{3+}_{1.55}R^{2+}_{0.45})O_{10}(OH)_2$ or $M^+_{0.60}(Si_4)(R_{1.4}R^{2+}_{0.60})O_{10}(OH)_2$, respectively, where $M^+ = (\frac{1}{2}Ca, Na)$,
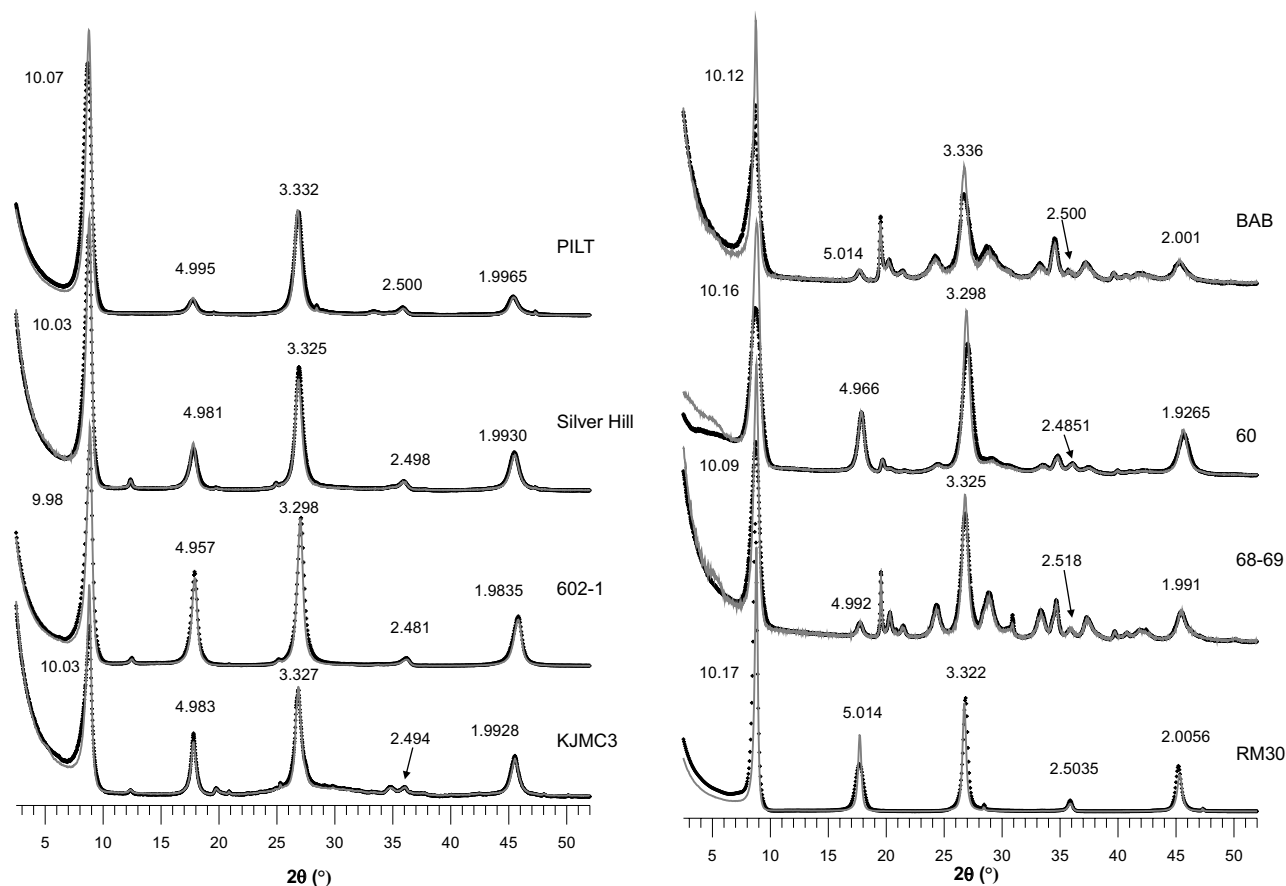

FIGURE 2. Comparison of XRD patterns from oriented specimens from air-dried and heated (shaded line) treatments (see text).

TABLE 3. Chemical composition of the studied samples

Sample	SiO_2	TiO_2	Al_2O_3	Fe_2O_3	FeO	MgO	CaO	Na_2O	K_2O	Sum
RM30	48.9		33.0			1.38	0.0	0.1	9.32	92.7
M422	48.62	0.30	34.48	0.16	0.10	0.91	0.3	0.06	8.80	93.73
10564	50.2	0.08	33.7	0.8		1.5	0.2	0.11	8.59	95.19
Silver Hill	50.47		24.45	4.83	1.45	2.11	0.06	0.36	8.22	91.95
KJMC3	51.77		24.99	1.41	1.91	3.16	0.16	0.48	7.93	91.81
Zempleni	51.21		29.77	0.24		2.21	0.35	0.22	7.71	91.71
60	53.81	0.19	21.35	3.24	1.96	3.97	0.25	0.07	8.62	93.56
602-1	53.02		20.31	0.82	1.48	4.91	0.12	0.24	8.23	89.13
136	54.06		12.40	2.34	3.08	5.42			8.24	85.60
69	54.30	0.09	1.30	21.04	5.86	3.80	0.44	0.01	8.99	95.7
TAIH	50.84		5.03	19.35	2.28	6.1		1.24	8.75	93.59
Z1	55.2		1.06	17.78	4.33	6.83	0.91		9.73	95.84
68-69	51.02	0.07	7.86	16.53	4.96	3.58	0.08	0.19	8.58	92.87
PILT	49.0		8.0	16.04	2.29	4.26		0.07	8.04	87.64
BAB	48.76	0.12	10.94	17.09	2.16	4.0	0.46	0.06	8.08	91.67

$R^{3+} = (Al, Fe^{3+})$, $R^{2+} = (Mg, Fe^{2+})$. The amounts of Fe^{3+} and Fe^{2+} are also assumed to be the same in the average and illite mica-like formulae. Each sample containing smectite layers is therefore characterized by a particular structural formula for the smectite layer. Taking into account the relatively low contents of expandable layers in these samples the mole contribution of the smectite component to the mean structural formula of each sample can be shown to be almost equal to the proportion of expandable layers. The mole contribution of smectite layers to the Zempleni sample formula is therefore assumed to be 15%, 10% for M422, and 3–5% for the other smectite-bearing samples. The corresponding mole contribution of the smectite layers into the average structural formula of each smectite-bearing sample was subtracted, and Table 4 contains, along with the average formulae, the structural formulae for the mica-like components. Note that the structural formulae of the mica-like components are similar to the average structural formulae of the corresponding samples.

Table 4 and Figure 3 show that according to the structural formulae the mica structures fall into two groups. One of them includes structures forming a solid solution from Al-rich illite to aluminoceladonite via Mg-rich illite. Samples RM30, 10564, and M422 are Al-rich illite because Al is the prevailing octahedral cation (1.86–1.96 cations per phfu). The deficiency of interlayer K, which is typical for illite, is compensated by lower Al for Si substitution (0.73–0.85 cations per phfu) as compared to ideal muscovite. Sample 60 is an Mg-rich illite that has a phengite-like composition with a high Mg content (0.39 cations phfu) and relatively low Al for Si substitution (0.39 cations phfu). The composition of this sample is not ideal phengite because it contains a significant amount of octahedral Fe^{3+} and Fe^{2+} (0.17 and 0.11 cations phfu, respectively). Heterogeneous octahedral cation composition is typical for all the samples in this group.

The Silver Hill and KJMC3 samples have cation compositions intermediate between that of the RM30 and 60 samples (Table 4; Fig. 3). Sample 136 has an aluminoceladonite-like cation composition with no tetrahedral Al, and the Mg and Fe^{2+} contents are 0.60 and 0.19 cations phfu, respectively. The cation composition of sample 602-1 is intermediate between those of samples 60 and 136 (Table 4). Thus, this collection of micaceous structures represents the most important members in the solid-solution Al-rich illite–Mg-rich illite–aluminoceladonite.

The second group of the samples forms a solid solution from typical glauconite to pure celadonite (Table 4). In these samples, Fe^{3+} is the dominant octahedral cation, and the contents of tetrahedral Al cations phfu decrease from samples BAB (0.44) to samples 68-69 (0.28), PILT (0.28), and TAIH (0.28), followed by the celadonite samples Z1 (0.04) and 69 (0.06). The sample TAIH is different in that it contains a significant amount of Na (0.18 atoms phfu) among the fixed interlayer cations (Table 4). These compositional features of the samples are taken into account in comparing the structural parameters within the glauconite-celadonite series.

STRUCTURE MODELING

The mica structural unit thickness ($c\sin\beta$ for the 1*M* polytype) corresponds to the octahedral and tetrahedral sheet thicknesses and the interlayer distance. Because the adjacent OH groups forming a shared octahedral edge are shifted toward each other along c^* by Δ_{OH} to provide shorter M-OH bonds and better screening for the repulsion of octahedral cations (Drits et al. 2006), the octahedral sheet is characterized by two thickness values, $<h_{oct}>$ and h_{oct}^{max}. Here h_{oct}^{max} is the distance along c^* between the upper and lower apical (i.e., non-hydroxyl) O atoms in an

TABLE 4. Cation compositions per $O_{10}(OH)_2$ of the studied samples and their mica components

| Sample	Component	Tetrahedral		Octahedral				Interlayer			Component proportion
		Si	Al	Al	Fe^{3+}+Ti	Fe^{2+}	Mg	K	Ca	Na	
RM30	average	3.27	0.73	1.86			0.14	0.80	0.03	0.01	
	illite	3.24	0.76	1.88			0.13	0.84	0.02	0.01	95%
M422	average	3.22	0.78	1.92	0.01		0.09	0.74	0.03		
	illite	3.15	0.85	1.96	0.01		0.05	0.83			90%
10564	illite	3.27	0.73	1.86	0.04		0.15	0.71	0.01	0.01	100%
Silver Hill	average	3.48	0.52	1.46	0.25	0.08	0.22	0.72		0.05	
	illite	3.46	0.54	1.47	0.25	0.08	0.21	0.76		0.02	95%
KJMC3	average	3.53	0.47	1.54	0.07	0.11	0.32	0.69	0.01	0.06	
	illite	3.51	0.49	1.54	0.07	0.11	0.32	0.73	0.01	0.04	95%
60	average	3.64	0.36	1.35	0.17	0.11	0.40	0.74	0.02	0.01	
	illite	3.62	0.38	1.36	0.17	0.11	0.39	0.78		0.01	95%
Zempleni	average	3.43	0.57	1.78	0.01		0.22	0.66	0.03	0.03	
	illite	3.36	0.64	1.82	0.01		0.18	0.78			85%
602-1	alumino-celadonite	3.71	0.29	1.39	0.04	0.09	0.51	0.75	0.01	0.03	100%
136	alumino-celadonite	4.00		1.08	0.13	0.19	0.60	0.78		0.01	100%
69	celadonite	3.94	0.06	0.06	1.15	0.36	0.41	0.83	0.03	0.01	100%
TAIH	celadonite (Na)	3.72	0.28	0.16	1.07	0.10	0.71	0.82		0.18	100%
Z1	celadonite	3.96	0.04	0.05	0.96	0.26	0.73	0.89		0.07	100%
68-69	average	3.73	0.27	0.43	0.92	0.30	0.39	0.80	0.01	0.03	
	glauconite	3.72	0.28	0.43	0.92	0.30	0.38	0.84		0.01	95%
BAB	average	3.58	0.42	0.53	0.94	0.13	0.44	0.76	0.04	0.01	
	glauconite	3.56	0.44	0.53	0.95	0.13	0.44	0.80	0.03	0.01	95%
PILT	average	3.73	0.27	0.44	0.93	0.21	0.47	0.75		0.05	
	glauconite	3.72	0.28	0.44	0.93	0.21	0.47	0.77		0.03	97%
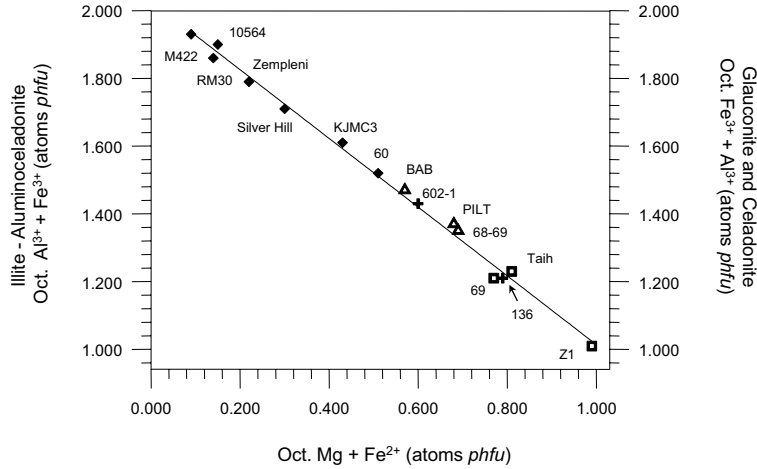
FIGURE 3. Relationships between Al,Fe³⁺ and Mg,Fe²⁺ octahedral cations in the illite-aluminoceladonite and glauconite-celadonite sample sequences. Symbols: diamond = illite, cross = aluminoceladonite, square = celadonite, triangle = glauconite.

octahedron, and $<h_{oct}>$ is the thickness of the octahedral sheet averaged over all the anions.

Because the vacant octahedra are larger than those occupied by cations, the adjacent tetrahedra are tilted across the elongated lateral edges of the vacant octahedra (Lee and Guggenheim 1981; Bailey 1984), so that the bridging basal oxygen moves inside the layer by ΔZ with respect to the other two basal O atoms of each tetrahedron. The tetrahedral sheet thickness is therefore characterized by two values, h_T^{max} and $<h_T>$, as calculated over the non-depressed and all basal O atoms, respectively. Accordingly, the thickness of the 2:1 layer is described by the values $<h_{TOT}> = h_{oct}^{max} + 2<h_T>$ and $h_{TOTt}^{max} = h_{oct}^{max} + 2h_T^{max}$. The interlayer distance is therefore characterized by the values $<h_{int}> = c\sin\beta - <h_{TOT}>$ and $h_{int}^{min} = c\sin\beta - h_{TOT}^{max}$, where $<h_{int}>$ is the average interlayer distance and h_{int}^{min} is the distance between the non-depressed basal tetrahedral O atoms across the interlayer.

To obtain the above structural parameters, the atomic co-ordinates of the unit cell were modeled for all samples from the chemical composition and unit-cell parameters, using a modified version of the algorithm of Smoliar-Zviagina (1993). The algorithm is based on regression equations relating the structural features and chemical compositions of micas that were obtained from the analysis of published data on refined structures of micas of various compositions. As essentially no reliable refined structural data exist on 1*M* dioctahedral micas, the empirical relationships in question were mostly based on the data on dioctahedral 2*M*₁ mica structures. Some of the regression equations used by Smoliar-Zviagina (1993) have been modified to account for new high-precision refined structural data on dioctahedral micas published since 1993. These relationships are given below:

$$d_T = 1.6187 + 0.1600(Al_t/4)^{1.25}, \text{ e.s.d.} = 0.002 \text{ Å} \qquad (1)$$

where d_T is the mean tetrahedral bond length and Al_t is the amount of tetrahedral Al cations phfu.

$$d(\text{M-O,OH}) = (1.918Al_{oct} + 2.000Fe^{3+} + 2.100Fe^{2+} + 2.060Mg$$
$$+ 1.945Ti + 1.950Cr + 1.980Mn)/\Sigma_{oct}, \text{ e.s.d.} = 0.004 \text{ Å} \quad (2)$$

where $d(\text{M-O,OH})$ is the mean octahedral bond length, Al, Fe³⁺, etc., are the number of the corresponding octahedral cations phfu, and Σ_{oct} is the sum of octahedral cations phfu.

$$\Delta Z = (0.235 Al_{oct} + 0.054 Fe^{3+})/\Sigma_{oct}, \text{ e.s.d.} = 0.008 \text{ Å} \qquad (3)$$

The application of the structure modeling procedure to the samples in this study was based on the following assumptions: (1) the structural features of the 2:1 layer in 1*M* micas should be similar to those in 2*M*₁, so that the structural data modeled for the 1*M* mica structures should also have similar reliability; and (2) the presence of stacking faults resulting from random layer rotations by $n \cdot 60°$, as well as the presence of expandable interlayers should not significantly affect the unit-cell parameters and structural distortions. The modeled atomic coordinates and the main structural parameters of the studied micas are given in Tables 5 and 6.

RESULTS

The contributions of the octahedral and tetrahedral sheet thicknesses and interlayer distances to $d(001) = c\sin\beta$, are shown in Figures 4, 5, and 6. Figure 4a shows h_{oct}^{max} plotted against $d(001)$. Two separate but similar trends are observed for the two groups of samples. The lower the Al for Si substitution in the tetrahedral sheets, and the higher the Mg for Al substitution in the octahedral sheets of the 2:1 layers in the illite-aluminoceladonite series, the thicker the octahedral sheet. In particular, along the transition from Al-rich illite (sample RM30) to aluminoceladonite (sample 136) the $d(001)$ values decrease from 10.018 to 9.898 Å and the thicknesses of the octahedral sheets, h_{oct}^{max}, increase from 2.130 to 2.185 Å (Fig. 4a; Table 6). The high Fe content in the glauconite-celadonite sample group increases the h_{oct}^{max} values significantly in comparison with those of the Al,Mg-rich samples. In the transition from Al-bearing glauconite (BAB) to almost Al-free celadonite (Z1), the $d(001)$ values decrease from 10.002 to 9.971 Å and the thicknesses of the octahedral sheet increase from 2.213 to 2.252 Å (Table 6). Thus, in the two groups, the decrease in the $d(001)$ value is accompanied by increasing the octahedral sheet thickness, h_{oct}^{max}.

TABLE 5. Modeled atomic coordinates of the unit cells for the mica structures

Sample	RM30			M422		
Atom	x	y	z	x	y	z
K	0.0000	0.5000	0.5000	0.0000	0.5000	0.5000
M	0.5000	0.1667	0.0000	0.5000	0.1667	0.0000
T	0.4191	0.3280	0.2688	0.4189	0.3279	0.2690
O1	0.3487	0.3100	0.1063	0.3474	0.3086	0.1060
O2	0.4984	0.5000	0.3131	0.5013	0.5000	0.3123
O3	0.6715	0.2246	0.3350	0.6697	0.2229	0.3350
OH	0.4191	0.0000	0.1006	0.4188	0.0000	0.0998

Sample	Silver Hill			KJMC3			60		
Atom	x	y	z	x	y	z	x	y	z
K	0.0000	0.5000	0.5000	0.0000	0.5000	0.5000	0.0000	0.5000	0.5000
M	0.5000	0.1667	0.0000	0.5000	0.1667	0.0000	0.5000	0.1667	0.0000
T	0.4191	0.3291	0.2710	0.4190	0.3292	0.2711	0.4198	0.3291	0.2715
O1	0.3516	0.3124	0.1082	0.3523	0.3135	0.1082	0.3544	0.3156	0.1089
O2	0.4881	0.5000	0.3182	0.4859	0.5000	0.3184	0.4750	0.5000	0.3203
O3	0.6751	0.2299	0.3361	0.6757	0.2309	0.3359	0.6828	0.2374	0.3366
OH	0.4186	0.0000	0.1035	0.4197	0.0000	0.1043	0.4209	0.0000	0.1055

Sample	Zempleni			602-1			136		
Atom	x	y	z	x	y	z	x	y	z
K	0.0000	0.5000	0.5000	0.0000	0.5000	0.5000	0.0000	0.5000	0.5000
M	0.5000	0.1667	0.0000	0.5000	0.1667	0.0000	0.5000	0.1667	0.0000
T	0.4184	0.3281	0.2692	0.4182	0.3292	0.2716	0.4174	0.3298	0.2725
O1	0.3493	0.3108	0.1066	0.3544	0.3169	0.1091	0.3575	0.3209	0.1104
O2	0.4935	0.5000	0.3137	0.4777	0.5000	0.3205	0.4585	0.5000	0.3241
O3	0.6722	0.2267	0.3350	0.6779	0.2348	0.3369	0.6850	0.2442	0.3373
OH	0.4198	0.0000	0.1013	0.4198	0.0000	0.1064	0.4194	0.0000	0.1090

Sample	69			TAIH			Z1		
Atom	x	y	z	x	y	z	x	y	z
K	0.0000	0.5000	0.5000	0.0000	0.5000	0.5000	0.0000	0.5000	0.5000
M	0.5000	0.1667	0.0000	0.5000	0.1667	0.0000	0.5000	0.1667	0.0000
T	0.4205	0.3324	0.2738	0.4209	0.3324	0.2741	0.4225	0.3326	0.2737
O1	0.3629	0.3529	0.1129	0.3616	0.3243	0.1124	0.3647	0.3276	0.1129
O2	0.4531	0.5000	0.3315	0.4709	0.5000	0.3315	0.4505	0.5000	0.3324
O3	0.6912	0.2492	0.3354	0.6836	0.2406	0.3362	0.6956	0.2519	0.3356
OH	0.4062	0.0000	0.1114	0.4076	0.0000	0.1110	0.4085	0.0000	0.1129

Sample	68-69			PILT			BAB		
Atom	x	y	z	x	y	z	x	y	z
K	0.0000	0.5000	0.5000	0.0000	0.5000	0.5000	0.0000	0.5000	0.5000
M	0.5000	0.1667	0.0000	0.5000	0.1667	0.0000	0.5000	0.1667	0.0000
T	0.4209	0.3314	0.2728	0.4219	0.3314	0.2729	0.4221	0.3312	0.2726
O1	0.3600	0.3214	0.1113	0.3602	0.3216	0.1113	0.3585	0.3192	0.1106
O2	0.4542	0.5000	0.3278	0.4639	0.5000	0.3276	0.4731	0.5000	0.3265
O3	0.6929	0.2490	0.3352	0.6899	0.2448	0.3351	0.6863	0.2402	0.3350
OH	0.4119	0.0000	0.1092	0.4122	0.0000	0.1091	0.4127	0.0000	0.1078

Sample	10564		
Atom	x	y	z
K	0.5000	0.6528	0.5000
M1	0.5000	0.1667	0.0000
M2	0.0000	0.3333	0.0000
T1	0.4333	0.9921	0.2692
T2	0.9185	0.8205	0.2692
O1	0.4152	0.9986	0.1063
O2	0.3432	0.3079	0.1063
O3	0.9958	0.6571	0.3343
O4	0.1585	0.9371	0.3129
O5	0.6696	0.8817	0.3343
OH	0.8408	0.1900	0.1008

Figure 4b shows that the mean thickness of the tetrahedral sheet, $<h_T>$, decreases with decreasing $d(001)$ to form a unique interdependence for both the illite-aluminoceladonite and glauconite-celadonite sample series, although considerable scatter exists in the $<h_T>$ values. Remarkable features of the relationship are that, first, the Al-rich illite and Fe-rich glauconite samples have similar $<h_T>$ values, and second, the range of the $<h_T>$ variations for the samples is very narrow. For the illite-aluminoceladonite members, $<h_T>$ decreases from 2.220 Å for $d(001) = 10.024$ to 2.202 Å for $d(001) = 9.898$ Å, whereas for the glauconite-celadonite series the $<h_T>$ values change from 2.216 to 2.208 Å almost independent of $d(001)$ (Table 6). In contrast, the relationship between the maximum thickness of the tetrahedral sheets, h_T^{max}, and $d(001)$ values is characterized by different cross plots for the two groups of samples. An increase in tetrahedral Al is accompanied by a significant increase in h_T^{max} (Fig. 4c) from 2.245 Å for $d(001) = 9.898$ to 2.296 Å for $d(001) = 10.024$ Å for the Al-rich illite–aluminoceladonite series, and
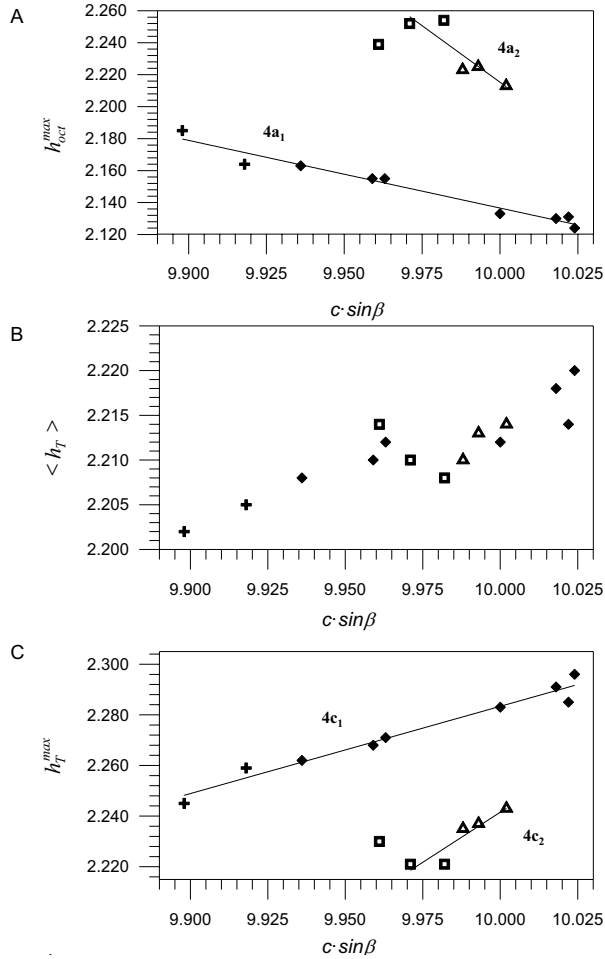
FIGURE 4. Relationships between $c\sin\beta$ and (**a**) maximal thickness of octahedral sheet, h_{oct}^{max}, (**b**) mean thickness of tetrahedral sheet, $<h_T>$, and (**c**) maximum thickness of tetrahedral sheet, h_T^{max}. Symbols: diamond = illite, cross = aluminoceladonite, square = celadonite, triangle = glauconite. Regression parameters: (4a$_1$) $h_{oct}^{max} = -0.423\ c\sin\beta + 6.37$, $R^2 = 0.963$, p-value <0.0001. (4a$_2$) $h_{oct}^{max} = -1.414\ c\sin\beta + 16.353$, $R^2 = 0.794$, p-value = 0.0422. (4c$_1$) $h_T^{max} = 0.345\ c\sin\beta - 1.163$, $R^2 = 0.962$, p-value <0.0001. (4c$_2$) $h_T^{max} = 0.791\ c\sin\beta - 5.673$, $R^2 = 0.860$, p-value = 0.0232.
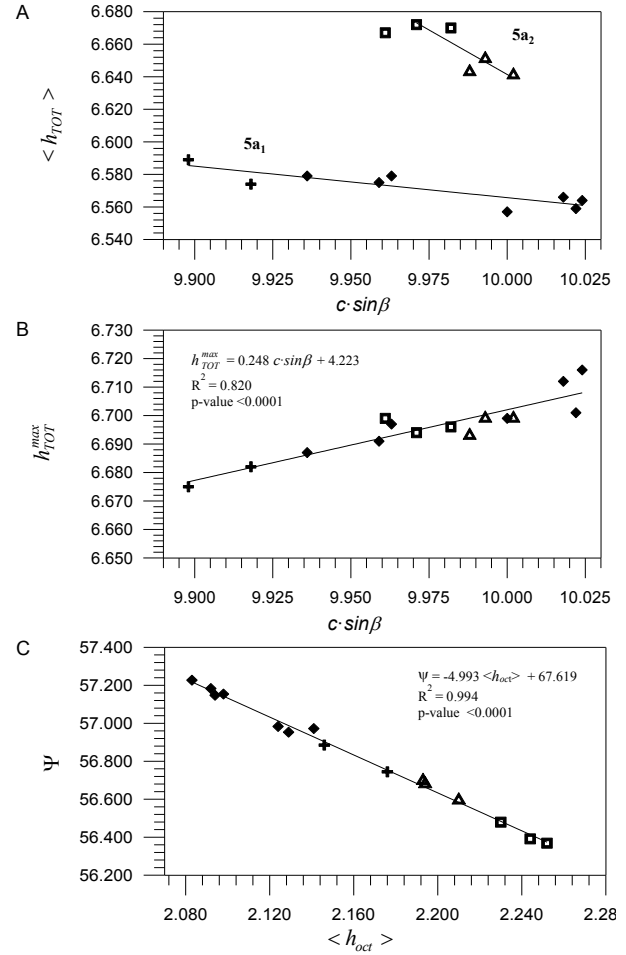
FIGURE 5. Relationships between $c\sin\beta$ and (**a**) the mean thickness of 2:1 layer, $<h_{TOT}>$, (**b**) the maximum thickness of 2:1 layer, h_{TOT}^{max}, and (**c**) the relationship between the flattening angle of the octahedral sheet, ψ, and the mean thickness of the octahedral sheet, $<h_{oct}>$. Symbols: diamond = illite, cross = aluminoceladonite, square = celadonite, triangle = glauconite. Regression parameters: (5a$_1$) $<h_{TOT}> = -0.193\ c\cdot\sin\beta + 8.501$, $R^2 = 0.758$, p-value = 0.0022. (5a$_2$) $<h_{TOT}> = -1.093\ c\sin\beta + 17.574$, $R^2 = 0.746$, p-value = 0.0590.

TABLE 6. Model parameters describing the structural features of octahedral and tetrahedral sheets and interlayer separation

Sample	$c\sin\beta$	h_{oct}^{max}	$<h_T>$	h_T^{max}	$<h_{TOT}>$	h_{TOT}^{max}	Ψ	$<h_{oct}>$	$<h_{int}>$	h_{int}^{min}	α_{mod}	ΔZ	$d(M_{tr}\text{-O})$	$d(M\text{-O})$	l_b
M422	10.024	2.124	2.220	2.296	6.564	6.716	57.227	2.083	3.460	3.308	11.20	0.179	2.260	1.933	2.654
10564	10.022	2.131	2.214	2.285	6.559	6.701	57.148	2.094	3.464	3.321	10.60	0.220	2.260	1.938	2.649
RM30	10.018	2.130	2.218	2.291	6.566	6.712	57.183	2.092	3.452	3.306	10.60	0.228	2.251	1.944	2.648
Zempleni	10.000	2.133	2.212	2.283	6.557	6.699	57.154	2.098	3.443	3.301	9.80	0.213	2.236	1.944	2.642
Silver Hill	9.963	2.155	2.212	2.271	6.579	6.697	56.983	2.124	3.384	3.266	8.50	0.175	2.238	1.958	2.637
KJMC3	9.959	2.155	2.210	2.268	6.575	6.691	56.953	2.129	3.384	3.268	8.20	0.214	2.228	1.962	2.635
60	9.936	2.163	2.208	2.262	6.579	6.687	56.972	2.141	3.356	3.249	5.70	0.162	2.216	1.977	2.629
602-1	9.918	2.164	2.205	2.259	6.574	6.682	56.885	2.146	3.344	3.236	6.70	0.162	2.199	1.976	2.625
136	9.898	2.185	2.202	2.245	6.589	6.675	56.745	2.176	3.309	3.223	3.00	0.130	2.171	1.999	2.614
BAB	10.002	2.213	2.216	2.243	6.645	6.699	56.680	2.194	3.357	3.301	4.50	0.086	2.201	2.008	2.631
68-69	9.993	2.225	2.213	2.237	6.651	6.699	56.595	2.210	3.344	3.294	1.10	0.075	2.186	2.019	2.622
PILT	9.988	2.223	2.210	2.235	6.643	6.693	56.697	2.193	3.345	3.295	2.80	0.075	2.182	2.008	2.624
69	9.982	2.254	2.208	2.221	6.670	6.696	56.392	2.244	3.312	3.286	1.00	0.038	2.147	2.041	2.614
Z1	9.971	2.252	2.210	2.221	6.672	6.694	56.369	2.252	3.299	3.277	0.03	0.032	2.132	2.047	2.614
TAIH	9.961	2.239	2.214	2.230	6.667	6.699	56.479	2.230	3.295	3.262	4.50	0.047	2.158	2.031	2.622

from 2.221 Å for $d(001) = 9.971$ to 2.243 Å for $d(001) = 10.002$ Å for the glauconite-celadonite series (Table 6).

Note that the position of sample TAIH deviates significantly from the trend observed for the glauconite-celadonite series (Figs. 4a–4c). The reason is that the interlayers of this sample contain 0.18 Na atoms phfu (Table 4). The presence of Na in dioctahedral micas promotes a decrease in the interlayer thickness (Guidotti et al. 1992). Similar deviations of the TAIH sample are observed for
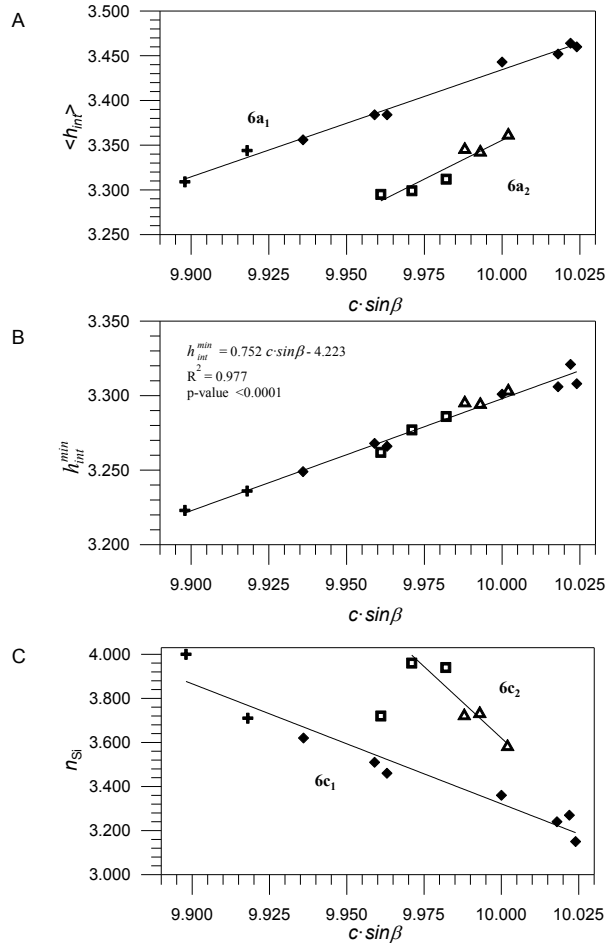
FIGURE 6. Relationships between $c\sin\beta$ and (**a**) the mean interlayer distance, $\langle h_{int}\rangle$, (**b**) minimum interlayer distance, h_{int}^{min}, and (**c**) the amount of tetrahedral Si. Symbols: diamond = illite, cross = aluminoceladonite, square = celadonite, triangle = glauconite. Regression parameters: (6a₁) $\langle h_{int}\rangle = 1.198\ c\sin\beta - 8.548$, $R^2 = 0.991$, p-value <0.0001. (6a₂) $\langle h_{int}\rangle = 1.740\ c\sin\beta - 14.043$, $R^2 = 0.991$, p-value = 0.0035. (6c₁) $n_{Si} = -5.447\ c\sin\beta + 57.789$, $R^2 = 0.939$, p-value <0.0001. (6c₂) $n_{Si} = -12.981 c\sin\beta + 133.428$, $R^2 = 0.880$, p-value = 0.0183.

relationships between $d(001)$ and other structural parameters.

The relationships between the mean thickness of the 2:1 layers, $\langle h_{TOT}\rangle$, and $d(001)$ (Fig. 5a) are similar to those found for the h_{oct}^{max} and $d(001)$ relationship (Fig. 4a). This cross plot consists of two trends which show a small increase in $\langle h_{TOT}\rangle$ with decreasing $d(001)$ for each of the sample groups. The similarity of the plots in Figures 5a and 4a results from the low sensitivity of the $\langle h_T\rangle$ values to the cation composition of the tetrahedral sheet (Fig. 4b). For the same reason, the $\langle h_{TOT}\rangle$ values for glauconite-celadonite are greater than those for the Al-rich illite–aluminoceladonite series. Moreover, because the variations in h_{oct}^{max} and $\langle h_T\rangle$ with decreasing $d(001)$ have opposite trends (Figs. 4a and 4b), the mean thickness of the 2:1 layers in the Al-rich illite–aluminoceladonite series is almost independent of the cation composition. For example, Table 6 and Figure 5a show that the $\langle h_{TOT}\rangle$ values increase only by about 0.02 Å from 6.566 to 6.589 Å in the solid solution from Al-rich illite (sample RM30) to aluminoceladonite (sample 136). For the glauconite-

celadonite samples, the $\langle h_{TOT}\rangle$ values vary over a slightly wider range, from 6.643 to 6.672 Å (Fig. 5a).

In contrast to two separate $\langle h_{TOT}\rangle$ vs. $d(001)$ trends for the illite-aluminoceladonite, and glauconite-celadonite sample groups, a unique, nearly linear relationship between the maximum thickness of 2:1 layers and $d(001)$ is observed for both groups of samples (Fig. 5b). Moreover h_{TOT}^{max} increases with increasing $d(001)$ by 0.037 Å, from 6.675 Å (sample136) to 6.712 Å (sample RM30) (Table 6). Because of the low sensitivity of the mean thickness of the 2:1 layers to their cation composition (Fig. 5a), the mean interlayer distance $\langle h_{int}\rangle$ decreases with decreasing $d(001)$ for both the Al-rich illite–aluminoceladonite and glauconite-celadonite series (Fig. 6a). In contrast to the separate trends for $\langle h_{int}\rangle$ vs. $d(001)$ observed for the two groups of samples, the h_{int}^{min} values form a unique and nearly linear relationship with $d(001)$ for both sample series (Fig. 6b).

DISCUSSION

In dioctahedral 2:1 layer silicates lateral adjustment of tetrahedral and octahedral sheets to form the 2:1 layer is achieved by flattening of the octahedral sheets along the c^* axis and counter-rotation of the upper and lower octahedra triads. Structural modifications of the tetrahedral sheet consist of corrugation of its basal surface, rotation of tetrahedra in the opposite direction around c^*, and their elongation along c^* (Bailey 1984). To reveal the main factors responsible for the crystal-chemical features of the studied structures, especially for the observed contraction of the mica structural unit, let us consider relationships between the structural parameters of the octahedral and tetrahedral sheets of the 2:1 layers and their interlayers.

Relationships between the octahedral sheet thickness and flattening

In general, the thickness of the octahedral sheet in the 2:1 layer depends on its cation composition, and the higher the oxidation state and the smaller the size of the octahedral cation, the thinner the octahedral sheet. The evolution of this thickness observed for the Al-rich illite–aluminoceladonite series is in agreement with this regularity (Fig. 4a). Indeed, in this sample group, substitution of the smaller trivalent octahedral Al cations by larger divalent Mg cations is accompanied by an increase in the octahedral sheet thickness, h_{oct}^{max}. A similar regularity exists for the glauconite-celadonite group (Fig. 4a).

Because the octahedral sheet is characterized by two thickness values, $\langle h_{oct}\rangle$ and h_{oct}^{max}, the octahedral sheet flattening may be characterized by two ψ angles calculated from the average d(M-O, OH) and d(M-O) bond lengths, where d(M-O) is the mean distance between the octahedral cation and apical oxygen anions. Thus:

$$\langle\psi\rangle = \arccos[\langle h_{oct}\rangle/2d(\text{M-O,OH})] \text{ and}$$
$$\psi_{max} = \arccos[h_{oct}^{max}/2d(\text{M-O})]. \qquad (4)$$

The relationship between $\langle\psi\rangle$ and $\langle h_{oct}\rangle$, and that between ψ_{max} and h_{oct}^{max} are quite different. The decrease in the $\langle h_{oct}\rangle$ values from aluminoceladonite to Al-rich illite, and from celadonite to Fe-rich glauconite leads to increasing $\langle\psi\rangle$ values (Fig. 5c), that is, to flattening the octahedral sheet. This trend can be described

by a unique linear regression equation:

$$<\psi> = 67.619 - 4.993 <h_{oct}>, \text{ e.s.d.} = 0.025°. \quad (5)$$

In contrast to the relationships between $<\psi>$ and $<h_{oct}>$, an increase in the h_{oct}^{max} values in the Al-rich illite–aluminoceladonite series is accompanied by only a slight increase in ψ_{max} from 56.70° for the Al-rich sample RM30, to 56.87° for the aluminoceladonite-like sample 136. For the glauconite-celadonite series the values of ψ_{max} also vary within a narrow range (56.48–56.60°). Therefore, the steady increase in the octahedral flattening in the aluminoceladonite–Al-rich illite and celadonite-glauconite groups is mostly associated with the shortening of shared OH-OH edges. In these structure sequences, the d(M-O) bond lengths and the h_{oct}^{max} values increase almost proportionally (Fig. 7a) because the range of ψ_{max} variation is small.

Relationships between the sizes of the vacant *trans*- and occupied *cis*-octahedra and the basal surface corrugation, ΔZ, of the tetrahedral sheet

In the mica structure, the vacant *trans*-octahedra are larger than occupied *cis*-octahedra. Because the adjacent tetrahedra across the elongated edges of *trans*-octahedra are tilted, the bridging basal oxygen moves inside the layer by ΔZ. The two regression lines in Figure 7b show that the larger the vacant *trans* octahedron, the higher the ΔZ values in each group of samples. The d(M-O) and ΔZ values are also related by two almost parallel linear dependences (Fig. 7c). However, in this case, the higher d(M-O), the smaller ΔZ. Thus, basal surface corrugation, ΔZ, of the tetrahedral sheet is determined by the difference in the lateral sizes of the *trans*- and *cis*-octahedra. The smaller the average distance from the center of the vacant *trans*-octahedron to its apices, d(M$_{tr}$-O), and the higher the d(M-O) bond length, or the smaller difference between these values, the smaller is the ΔZ value. For example, the difference between the d(M$_{tr}$-O) and d(M-O) distances for the Al-rich illite in sample RM30 (2.251 – 1.944 = 0.307 Å) and the aluminoceladonite-like Mg, Fe^{2+}-rich sample 136 (2.171 – 1.999 = 0.172 Å) shows that with increasing substitution of Mg and Fe^{2+} for Al the sizes of the occupied *cis*- and vacant *trans*-octahedra become closer (Table 6). A similar effect is observed for the glauconite-celadonite samples (Table 6). This means that the transitions from illite to aluminoceladonite as well as from glauconite to celadonite are accompanied by a steady decrease in ΔZ. Note that the relationships shown in Figures 7a and 7c may explain the almost linear dependence between ΔZ and h_{oct}^{max}, which is unique for all the studied samples (Fig. 8a).

Influence of the basal surface corrugation, ΔZ, on the mean and maximum thickness of the tetrahedral sheet

In the transition from Al-rich illite to aluminoceladonite, as well as from glauconite to celadonite, the size of the vacant *trans*-octahedra decreases as does the Al content in the tetrahedral sheets. Such a transition should therefore decrease both h_T^{max} and ΔZ. The two regressions in Figure 8b correspond to the following equations:

$$h_{T_1}^{max} = 2.180 + 0.497 \, \Delta Z_1 \text{ and } h_{T_2}^{max} = 2.207 + 0.402 \, \Delta Z_2, \text{ or}$$

$$\Delta Z_1 = 2.012 \, h_{T_1}^{max} - 4.386 \text{ and } \Delta Z_2 = 2.488 \, h_{T_2}^{max} - 5.490. \quad (6)$$

Here ΔZ_1 and ΔZ_2 are the ΔZ values for the Al-rich illite–aluminoceladonite, and glauconite-celadonite groups, respectively. The mean thickness of the tetrahedral sheet is $<h_T> = (3 \, h_T^{max} - \Delta Z)/3$. Taking into account the regressions for ΔZ_1 and ΔZ_2 (Eq. 6), the mean thickness of the tetrahedral sheets for the two groups of samples ($<h'_T>$ and $<h''_T>$, respectively) are

$$<h'_T> = 0.33 \, h_T^{max} + 1.461 = 2.180 + 0.164 \, \Delta Z_1, \text{ and}$$
$$<h''_T> = 0.172 \, h_T^{max} + 1.828 = 2.207 + 0.069 \, \Delta Z_2. \quad (7)$$

Significant variations in the h_T^{max} values in both sample series (Fig. 4c) are determined by their strong dependence on ΔZ

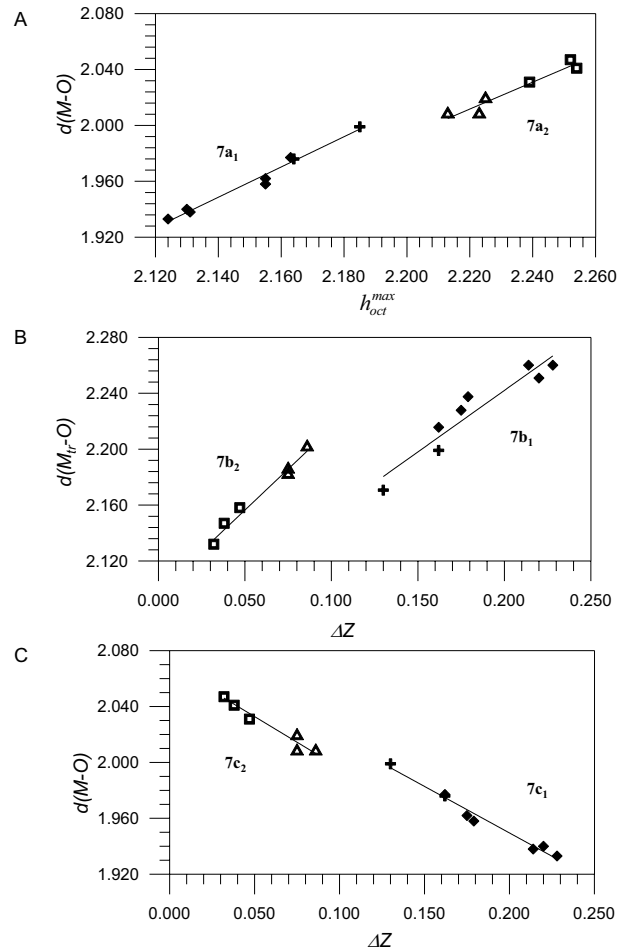**FIGURE 7.** Relationships between (**a**) octahedral bond length (M-O) and maximum thickness of the octahedral sheet, h_{oct}^{max}, (**b**) octahedral distance from the center of the vacant trans site (M$_{tr}$-O) to the nearest oxygen atoms, and corrugation of basal oxygen surface, ΔZ, and (**c**) octahedral bond length (M-O) and corrugation of basal oxygen surface, ΔZ. Symbols: diamond = illite, cross = aluminoceladonite, square = celadonite, triangle = glauconite. Regression parameters: (7a$_1$) d(M-O) = 1.084 h_{oct}^{max} – 0.370, R^2 = 0.978, p-value < 0.0001. (7a$_2$) d(M-O) = 0.962 h_{oct}^{max} – 0.123, R^2 = 0.933, p-value = 0.0075. (7b$_1$) d(M$_{tr}$-O) = 0.880 ΔZ + 2.066, R^2 = 0.907, p-value = 0.0003. (7b$_2$) d(M$_{tr}$-O) = 1.173 ΔZ + 2.098, R^2 = 0.983, p-value = 0.0009. (7c$_1$) d(M-O) = -0.666 h_{oct}^{max} + 2.083, R^2 = 0.977, p-value < 0.0001. (7c$_2$) d(M-O) = –0.734 h_{oct}^{max} + 2.070, R^2 = 0.951, p-value = 0.0047.
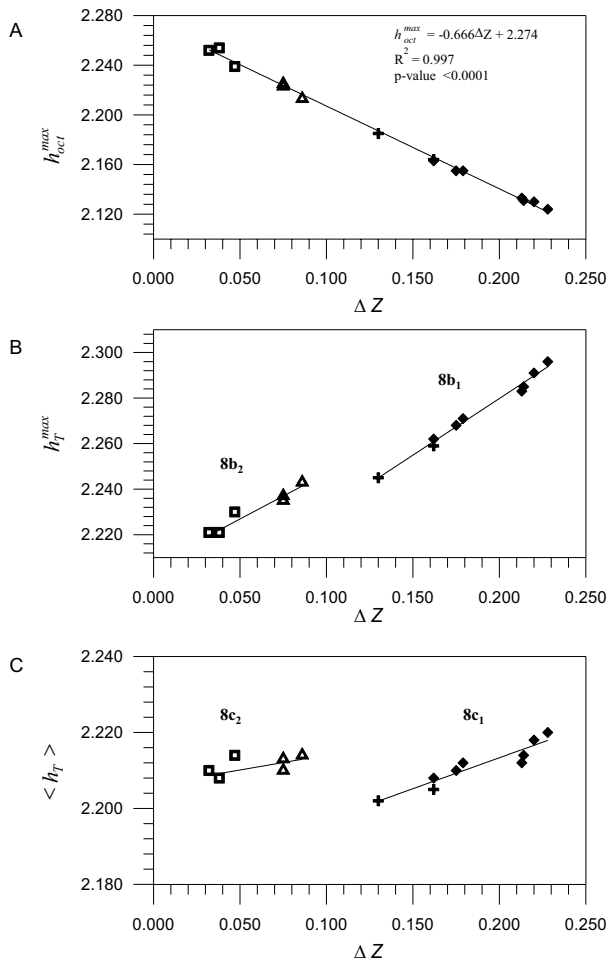
FIGURE 8. Relationships between corrugation of basal oxygen surface, ΔZ, and (**a**) the maximum thickness of the octahedral sheet, h_{oct}^{max}, (**b**) maximum thickness of the tetrahedral sheet, h_T^{max}, and (**c**) the mean thickness of the tetrahedral sheet, $<h_T>$. Symbols: diamond = illite, cross = aluminoceladonite, square = celadonite, triangle = glauconite. Regression parameters: ($8b_1$) $h_{oct}^{max} = 0.497\,\Delta Z + 2.180$, $R^2 = 0.987$, p-value < 0.0001. ($8b_2$) $h_{oct}^{max} = 0.402\,\Delta Z + 2.207$, $R^2 = 0.976$, p-value = 0.0016. ($8c_1$) $<h_T> = 0.163\,\Delta Z + 2.181$, $R^2 = 0.884$, p-value = 0.0002. ($6c_2$) $<h_T> = 0.078\,\Delta Z + 2.206$, $R^2 = 0.610$, p-value = 0.1186.

(Eq. 6), that is, by the difference in the sizes of the *trans*- and *cis*-octahedra. Averaging the positions of depressed and non-depressed basal O atoms of the tetrahedral sheets dramatically decreases the dependence of $<h_T>$ on ΔZ (Eq. 7; Fig. 8c). Therefore, lateral adjustment of octahedral and tetrahedral sheets in the 2:1 layers does not change the $<h_T>$ values in the glauconite-celadonite sample group, and only slightly decreases the $<h_T>$ values by about 0.02 Å in the Al-rich illite–aluminoceladonite series (Table 6).

Empirical equations for determination of the tetrahedral rotation angle α

The rotation of adjacent tetrahedra around the c^* axis by the α angle that allows the lateral adjustment of the octahedral and tetrahedral sheets depends on many structural parameters of both

sheets (Smoliar-Zviagina 1993; Brigatti and Guggenheim 2002). In general, substitution of smaller trivalent for larger divalent octahedral cations and the simultaneous decrease in the tetrahedral Al content improves the fit between the sheets and consequently decreases the tetrahedral rotation angle α.

Analysis of the published data (Brigatti and Guggenheim 2002 and references therein) on refined $2M_1$ dioctahedral mica structures yields the equation:

$$\cos\alpha = b/(9.028 + 0.169\,Al_t), \quad \text{e.s.d.} = 0.7°. \tag{8}$$

For the illite-aluminoceladonite, and glauconite-celadonite samples, the following relationships are valid for the α values obtained from structure modeling:

$$\cos\alpha = b/(9.028 + 0.155\,Al_t), \text{ and}$$
$$\cos\alpha = b/(9.045 + 0.124\,Al_t), \quad \text{e.s.d.} = 0.4°. \tag{9}$$

Brigatti and Guggenheim (2002) suggested that tetrahedral rotation in micas was related to the ratio of basal tetrahedral and lateral octahedral edge lengths so that $\cos\alpha = (\sqrt{3}/2)k$, where k is the ratio of the mean octahedral lateral O-O distance (taking into account the vacant octahedron) to the mean basal tetrahedral edge length. Figures 13 and 14 in Brigatti and Guggenheim (2002) show that for the range of α values from about 5° to about 10°, the scatter of the points is up to 3° when the observed edge lengths are used, and up to 6–8° using the empirical relationships suggested by the authors. For the samples in this study, this relationship underestimates the modeled α values by 1 to 2°. Using the equations $\cos\alpha = 0.8637k$ and $\cos\alpha = 0.8646k$ for illite-aluminoceladonite and glauconite-celadonite samples, respectively, improves the accuracy to 0.4 and 0.95°. Even better results are obtained using the equations

$$\cos\alpha = 0.868b/3l_b, \quad \text{e.s.d.} = 0.4° \text{ and}$$
$$0.8664b/3l_b, \quad \text{e.s.d.} = 0.3° \tag{10}$$

where l_b is the mean basal tetrahedral edge for illite-aluminoceladonite and glauconite-celadonite samples. Figures 9a–9c demonstrate the correlations between the α values calculated by Equations 8–10, and the observed α relationships for $2M_1$ structures and the modeled α value relationship for the samples in this study. The perfect correlation between the α values calculated from the atomic coordinates and from Equation 9 using the b parameter and the amount of tetrahedral Al cations phfu can be considered as indirect evidence of the reliability of the modeled structural parameters.

Statistical significance of the regression equations

The above described regressions (Figs. 4–9) are evaluated for statistical significance by the coefficient of determination, R^2, and the Anova quality of fit p-value. Two types of regressions can be distinguished. One corresponds to the relationships between the structural parameters of both sample groups that are described by a single equation. These regressions are shown in Figures 5b, 5c, 6b, 8a, and 9. For this regression type the R^2 parameter varies from 0.918 to 0.997 and the p-values are <0.0001. The only exception is the relationship between h_{TOT}^{max} and $c\sin\beta$, for
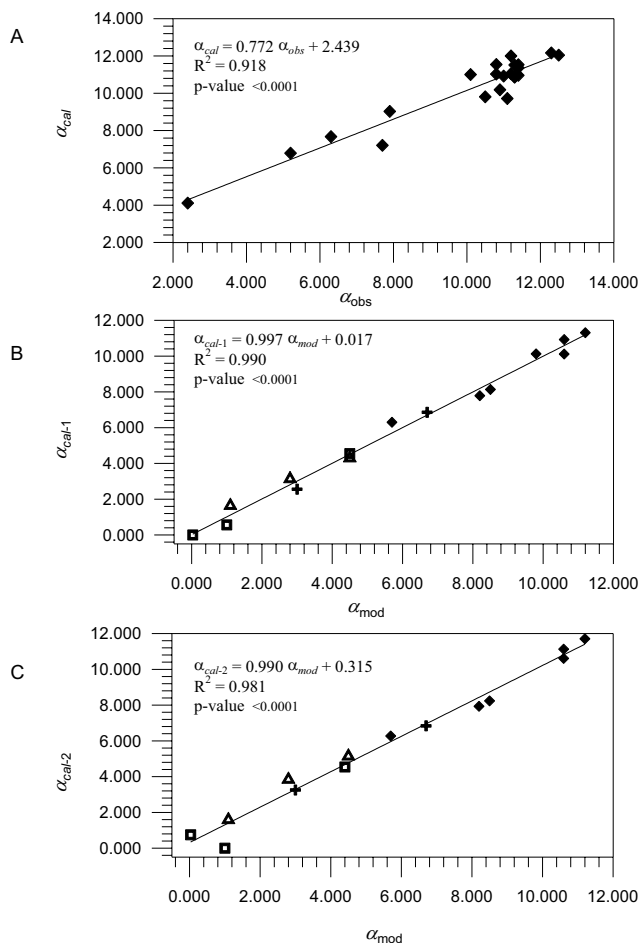
FIGURE 9. The correlations between the calculated α values and (**a**) the observed α for 2M_1 structures, and, (**b–c**) the modeled α value for the samples (see text). Symbols: diamond = illite, cross = aluminoceladonite, square = celadonite, triangle = glauconite.

which $R^2 = 0.820$.

The second type of regression corresponds to the relationship between parameters of either the illite-aluminoceladonite or glauconite-celadonite sample group. The regressions describing the relationships between the structural parameters of the illite-aluminoceladonite sample series have the same significance level as those for the single regressions determined for both sample groups, where the R^2 values are between 0.907–0.991 and the p-values are <0.0001. The regressions corresponding to the relationships $<h_{\mathrm{TOT}}>$ vs. $c\sin\beta$ (Fig. 5a$_1$) and $<h_T>$ vs. ΔZ (Fig. 8c$_1$) are exceptions, with R^2 of 0.758 and 0.883, and p-values of 0.0022 and 0.0002, respectively.

The regressions describing the glauconite-celadonite sample group can be divided into three subgroups. The first describes the relationships between various structural parameters of the 2:1 layers (Figs. 7a$_2$, 7b$_2$, 7c$_2$, and 8b$_2$), as well as that between $<h_{\mathrm{int}}>$ and $c\sin\beta$ (Fig. 6a$_2$), that is, the regressions where the $c\sin\beta$ values are not related to the structural parameters of the 2:1 layers. For these regressions the R^2 values are between 0.88 and 0.991 and the p-values are <0.007.

The second regression subgroup corresponds to the relationships between $c\sin\beta$ and the structural parameters of the 2:1

layers (Figs. 4a$_2$, 4c$_2$, and 6c$_2$), which are characterized by both low R^2 (0.74–0.88) and relatively higher p-values (0.018–0.042). These values still represent an acceptable significance because a common p-value threshold for a significant difference between means is 0.05.

The third group of regressions describes the relationships between $<h_{\mathrm{TOT}}>$ and $c\sin\beta$, as well as between $<h_T>$ and ΔZ (Figs. 5a$_2$ and 8c$_2$). The p-values for these regressions are 0.059 and 0.1186, respectively, and exceed the accepted significance threshold of 0.05. The reason is the combination of the small number of samples, low sensitivity of $<h_T>$ and $<h_{\mathrm{TOT}}>$ to variations in ΔZ and $c\sin\beta$, respectively, and the considerable scatter in the parameter values.

### New interpretation for the observed contraction of the mica structural unit

As shown above, the $<h_{\mathrm{TOT}}>$ values do not decrease, but increase slightly with increasing contents of octahedral Mg and Fe^{2+} cations. In the Al-rich illite–aluminoceladonite series $<h_{\mathrm{TOT}}>$ increases from 6.564 to 6.589 Å, and in the glauconite-celadonite group, from 6.645 to 6.672 Å. Therefore the decrease in the $d(001)$ values from 10.024 to 9.886 Å, and from 10.002 to 9.971 Å in these respective groups is determined mostly by the decreasing mean interlayer distance (Figs. 6a). The simplest and generally accepted model is that the tetrahedral rotation is the main factor responsible for the interlayer contraction in muscovite-phengite structures, where the smaller the α angle, the larger the size of the ditrigonal ring and interlayer cavity, and the more favorable the conditions for the contraction of the interlayer space, which minimizes the average K-O$_b$ distances, as well as the differences between the (K-O$_b$)$_{\mathrm{inner}}$ and (K-O$_b$)$_{\mathrm{outer}}$ (Sokolova et al. 1976; Massonne and Schreyer 1986; Schmidt et al. 2001; Ivaldi et al. 2001; Ferraris and Ivaldi 2002).

A new insight into the interpretation of the contraction of the mica layer in dioctahedral 1M micas can be achieved if we take into account that the mean interlayer distance depends primarily on Al for Si substitution. The increase in the amount of tetrahedral Al leads to undersaturation of the basal O atoms with respect to negative charge and consequently to their mutual repulsion (Takeda et al. 1971). Therefore the greater the tetrahedral Al for Si substitution the stronger the repulsion between the planes of basal O atoms and the larger is the interlayer distance. According to this concept, the basal O atoms that have the same average under-saturated negative charge should be separated by the same mean interlayer distance and vice versa.

The validity of this interpretation is supported by the comparison of mica pairs in which the members of each pair have the same or nearly the same $<h_{\mathrm{inter}}>$ values, but belong to different groups of samples, one to the Al-rich–aluminoceladonite group, and the other to the glauconite-celadonite group (Table 7; Figs. 10a–10c). For example, the aluminoceladonite sample (136) and celadonite sample (Z1), as well as the Mg-rich illite sample (60) and the glauconite sample (BAB), have identical or very similar mean interlayer thicknesses and Al for Si substitutions in the tetrahedral sheets. In particular, for the first pair, the $<h_{\mathrm{int}}>$ values are 3.309 and 3.299 Å, and the Al$_r$ values are 0.00 and 0.04 atoms phfu, respectively. For the second pair the $<h_{\mathrm{int}}>$ values are 3.356 and 3.357 Å and the Al$_t$ values are 0.38 and

TABLE 7. Sample groups having the same or close mean interlayer separation and Al for Si substitution, but different interlayer structure

Sample	Z1	136	68-69	602-1	BAB	60
Al_T (pfu)	0.040	0.030	0.280	0.290	0.440	0.380
$<h_{int}>$ (Å)	3.299	3.309	3.344	3.344	3.357	3.356
α_{mod}°	0.03	3.00	1.10	6.70	4.50	5.70
ΔZ (Å)	0.032	0.130	0.075	0.162	0.086	0.162
h_{int}^{max} (Å)	0.343	3.481	3.442	3.560	3.471	3.573
H_{int}^{min} (Å)	3.277	3.223	3.294	3.236	3.301	3.249
$(K-O)_{inner}$ (Å)	3.341	3.002	3.109	2.949	3.016	2.982
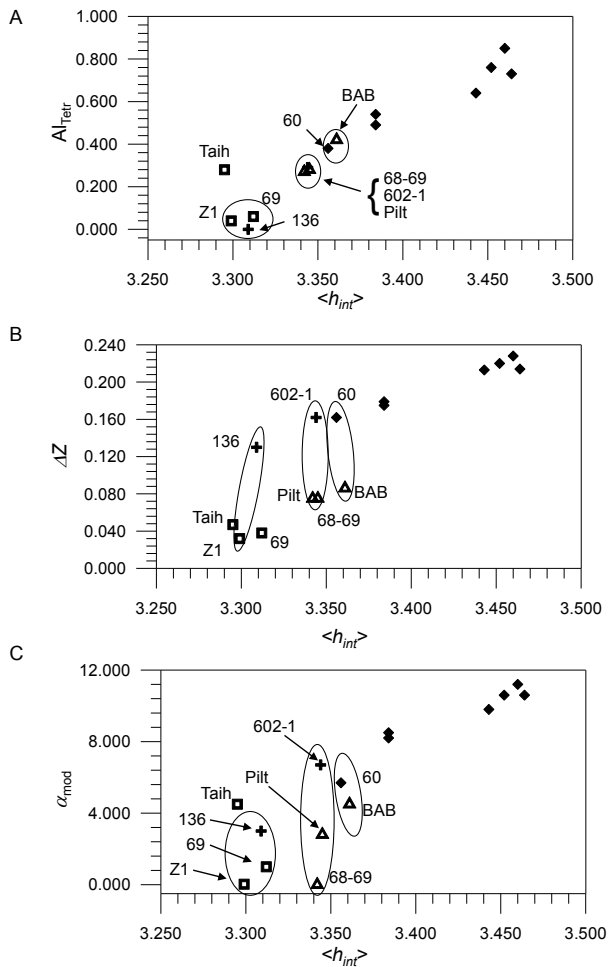
FIGURE 10. Relationships between the mean interlayer distance, $<h_{int}>$, and (**a**) the amount of tetrahedral Al, (**b**) corrugation of basal oxygen surface, ΔZ, and (**c**) the modeled ditrigonal rotation angle, α (see text). Symbols: diamond = illite, cross = aluminoceladonite, square = celadonite, triangle = glauconite.

0.44 atoms phfu, respectively (Fig. 10a). However, Table 7 and Figures 10b–10c show that the interlayer structures of each pair have different α, ΔZ, h_{inter}^{min}, and h_{inter}^{max} values. As a result, the distortions of the K-bearing polyhedra are different for each member of the pair. For example, the interlayer structures of samples 136 and Z1 have significantly different α values (3.0 vs. 0.03°), ΔZ (0.130 vs. 0.03 Å), h_{inter}^{min} (3.223 vs. 3.277 Å), and h_{inter}^{max} (3.481 vs. 3.343 Å). Similarly, the interlayer structures of samples 60 and BAB have significantly different parameters (Table 7; Fig. 10). The two samples aluminoceladonite 602-1 and glauconite 68-69,

which occupy an intermediate position between the above two pairs of samples, have identical Al_t contents (0.28 cations phfu) and $<h_{int}>$ (3.344 Å), but different parameters characterizing their interlayer structures (Table 7; Fig. 10).

As was mentioned for each sample group, the mean thickness of the 2:1 layers has low sensitivity to the cation composition (Fig. 5a) and the observed decrease in the $c\sin\beta$ value is determined by the decrease in $<h_{int}>$, which, in turn, depends on the substitution of Al for Si. Therefore, almost linear interdependences exist between Si and $c\sin\beta$ for both groups of samples (Fig. 6c).

Comparison of the interlayer structures of 1*M* illite consisting of *trans*-vacant and *cis*-vacant layers

The interlayer structures of *tv* and *cv* 1*M* Al-rich illite structures represented by samples RM30 and 10564, respectively, provide a remarkable example to support the crucial role of the repulsion of the adjacent basal O atoms of the tetrahedral sheets across the interlayer. The two structures have similar $c\sin\beta$ values of 10.018 and 10.022 Å, similar amounts of tetrahedral Al (0.76 and 0.73 apfu) and close values of $<h_{inter}>$ of 3.452 and 3.464 Å, respectively. In the *tv* structure, the nearest depressed basal O atoms of the adjacent tetrahedral sheets are located on the layer mirror planes, almost exactly one above the other along the c^* axis.

Therefore, in the *tv* structure of the RM30 sample, the interlayer K is located in a distorted prism in which two edges formed by the nearest depressed O atoms are significantly longer (3.816 Å) than the other four (3.356 Å) formed by the nearest non-depressed O atoms. In contrast, in the interlayer cavity of the *cv* 1*M* structure, the grooves formed by rows of the depressed basal O atoms of the adjacent tetrahedral sheets are rotated with respect to each other by 120° and, therefore, each depressed oxygen has a non-depressed oxygen atom as nearest neighbor (Drits et al. 2006). As a result, the edge lengths of the interlayer prism are partly equalized in the *cv* 1*M* structure in such a way that four edges become significantly shorter (3.586 Å) than the two longer ones formed by the depressed O atoms in the *tv* structure, and only two edges have the same lengths as the shorter ones in the *tv* 1*M* structure (3.356 Å). Therefore, although the layer and interlayer structures of the *tv* and *cv* Al-rich illite polymorphs differ significantly, the two structures have the same average interlayer distance and $c\sin\beta$ values because of the close average non-compensated negative charge of the basal oxygen anions.

REFERENCES CITED

Bailey, S.W. (1984) Crystal chemistry of the true mica. In S.W. Bailey, Ed., Micas, 13, p. 13–66. Reviews in Mineralogy, Mineralogical Society of America, Chantilly, Virginia.
Brigatti, M.F. and Guggenheim, S. (2002) Mica crystal chemistry and the influence of pressure, temperature and sold solution on atomistic models. In A. Mottana, F.E. Sassi, J.B. Thompson Jr., and S. Guggenheim, Eds., Micas: Crystal chemistry and metamorphic petrology, 46, p. 1–97. Reviews in Mineralogy

and Geochemistry, Mineralogy Society of America, Chantilly, Virginia, with Accademia Nazionale dei Lincei, Roma, Italy.

Drits, V.A. and Kossovskaya, A.G. (1991) Clay Minerals: Micas and Chlorites, 175 p. Nauka, Moscow (in Russian).

Drits, V.A. and McCarty, D.K. (2007) The nature of structure-bonded H_2O in illite and leucophyllite from dehydration and dehydroxylation experiments. Clays and Clay Minerals, 55, 45–58.

Drits, V.A. and Tchoubar, K. (1990) X-ray Diffraction by Disordered Lamellar Structures, 330 p. Springer-Verlag, Berlin.

Drits, V.A., Plançon, A., Sakharov, B.A., Besson G., Tsipursky, S.I., and Tchoubar, C. (1984) Diffraction effects calculated for structural models of K-saturated montmorillonite containing different types of defects. Clay Minerals, 19, 541–562.

Drits, V.A., Weber, F., Salyn, A., and Tsipursky, S.I. (1993a) X-ray identification of 1M illite varieties. Clays and Clay Minerals, 28, 185–207.

Drits, V.A., Kameneva, M.Yu., Sakharov, B.A., Dainyal, L.G., Smoliar, B.B., Bookin, A.S., and Salyn, A.L. (1993b) Problems in Determination of the Actual Crystal Structure of Glauconites and Related Phyllosilicates, 198 p. Nauka, Novosibirsk (in Russian).

Drits, V.A., McCarty, D.K., and Zviagina, B.B. (2006) Crystal-chemical factors responsible for the distribution of octahedral cations over *trans*- and *cis*-sites in dioctahedral 2:1 layer silicates. Clays and Clay Minerals, 54, 131–153.

Eberl, D.D., Środoń, J., Lee, M., Nadeau, P.H., and Northrop, H.R. (1987) Sericite from the Silverton Caldera, Colorado: Correlation among structure, composition, origin, and particle thickness. American Mineralogist, 72, 914–934.

Ferraris, G. and Ivaldi, G. (2002) Structural features of micas. In A. Mottana, F.E. Sassi, J.B. Thompson Jr., and S. Guggenheim, Ed., Micas: Crystal Chemistry and Metamorphic Petrology, 46, p. 117–153. Reviews in Mineralogy and Geochemistry, Mineralogy Society of America, Chantilly, Virginia, with Accademia Nazionale dei Lincei, Roma, Italy.

Guidotti, C.V., Mazzoli, C., Sassi, F.P., and Blencoe, J.G. (1992) Compositional controls on the cell dimensions of $2M_1$ muscovite and paragonite. European Journal of Mineralogy, 4, 283–297.

Güven, N. (1971) The crystal structures of $2M_1$ phengite and $2M_1$ muscovite. Zeitschrift für Kristallographie, 134, 196–212.

Ivaldi, G., Ferraris, G., Curetti, N., and Compagnoni, R. (2001) Coexisting 3T and $2M_1$ polytypes in a phengite from Cima Pal (Val Savenca, western Alps): Chemical and polytypic zoning and structural characterization. European Journal of Mineralogy, 13, 1025–1034.

Ivanovskaya, T.A., Tsipursky, S.I., and Yakovleva, O.V. (1989) Mineralogy of globular glauconites from Vendian and Rephean of the Ural and Siberia. Litologia and poleznye iskopaemye, 3, 83–99 (in Russian).

Kimbara, K. and Shimoda, S. (1973) A ferric celadonite in amygdales of dolerite at Taiheizan, Akita prefecture, Japan. Clay Science, 4, 143–150.

Kogure, T., Kameda, J., and Drits, V.A. (2008) Stacking faults with 180° layer rotation in celadonite: An Fe- and Mg-rich dioctahedral mica. Clays and Clay Minerals, 56, 612–621.

Lazarenko, E.K. and Pavlishin, V.I. (1976) Relationship of celadonite and svitalskite. In E.K. Lazarenko, Ed., Mineralogy of Sedimentary Rocks. No. 3. Naukova Dumka, Kiev (in Russian).

Lee, H.L. and Guggenheim, S. (1981) Single crystal refinement of pyrophyllite-1*Tc*. American Mineralogist, 66, 350–357.

Lee, P.L., Shu, D., Ramanathan, M., Preissner, C., Wang, J., Beno, M.A., Von Dreele, R.B., Ribaud, L., Kurtz, C., Antao, S.M., Jiao, X., and Toby, B.H. (2008) A twelve-analyzer detector system for high-resolution powder diffraction. Journal of Synchrotron Radiation, 15, 427–432.

Li, G., Peacor, D.R., Coombs, D.S., and Kawachi, Y. (1997) Solid solution in the celadonite family: The new minerals ferroceladonite $K_2Fe_2^{2+}Fe_2^{3+}Si_8O_{20}(OH)_4$ and ferroaluminoceladonite $K_2Fe_2^{2+}Al_2Si_8O_{20}(OH)_4$. American Mineralogist, 82, 503–511.

Malkova, K.M. (1956) On the celadonite of Pobuzhye. In E.K. Lazarenko, Ed., Collected Papers on Mineralogy, 10, 305–318. Lvov Geological Society, Lvov (in Russian).

Massone, H.J. and Schreyer, W. (1986) High pressure syntheses and X-ray properties of white micas in the system K_2O-MgO-Al_2O_3-H_2O. Neues Jahrbuch für Mineralogie, Abhandlungen, 153, 177–215.

——— (1989) Stability field of the high-pressure assemblage talc + phengite and two new phengite barometers. European Journal of Mineralogy, 1, 391–410.

Moore, D.M. and Reynolds Jr., R.C. (1997) X-ray Diffraction and the Identification and Analysis of Clay Minerals, 2nd edition. Oxford University Press, New York.

Nikolaeva, I.V. (1977) Minerals of the Glauconite Group in Sedimentary Formations, 319 p. Nauka, Novosibirsk (in Russian).

Petrova, V.V. and Amarjargal, P. (1996) Zeolites of Mongolia, 150 p. Nauka, Moscow (in Russian).

Reynolds Jr., R.C. (1992) X-ray diffraction study of illite-smectite from rocks, <1 μm randomly oriented powders, and <1 μm oriented powder aggregates: The absence of laboratory-induced artifacts. Clays and Clay Minerals, 40, 387–396.

Rieder, M., Cavazzini, G., D'yakonov, Y.S., Frank-Kamenetskii, V.A., Gottardi, G., Guggenheim, S., Koval, P.V., Muller, G., Neiva, A.M.R., Radoslovich, E.W., Robert J.-L., Sassi, F.P., Takeda, H., Weiss, Z., and Wones, D.R. (1998) Nomenclature of the micas. Clays and Clay Minerals, 46, 586–595.

Ryan, P.C., Coish, R., and Joseph, K. (2007) Ordovician K-bentonites in western Vermont: Mineralogic, stratigraphic, and geochemical evidence for their occurrence and tectonic significance. Geological Society of America Abstracts with Programs, 39(1), p. 50.

Sakharov, B.A., Besson, G., Drits, V.A., Kameneva, M.Y., Salyn, A.L., and Smoliar, B.B. (1990) X-ray study of the nature of stacking faults in the structure of glauconites. Clay Minerals, 25, 419–435.

Schmidt, M.W., Dugnani, M., and Artioli, G. (2001) Synthesis and characterization of white micas in the join muscovite-aluminoceladonite. American Mineralogist, 86, 555–565.

Shutov, V.D., Katz, M.Y., Drits, V.A., Sokolova, A.L., and Kazakov, G.A. (1975) Crystal chemistry of glauconites as an indicator of facial condition of their formation and postsedimentary transformation. In A.G. Kossovskaya, Ed., Crystal Chemistry of Minerals and Geological Problems, p. 74–81. Nauka, Moskow (in Russian).

Slonimskaya, M.V., Drits, V.A., Finko, V.I., and Salyn, A.L. (1978) The nature of interlayer water in fine-dispersed muscovites. Izvestiya Akademii Nauk SSSR, seriya geologicheskaya, 10, 95–104 (in Russian).

Smoliar-Zviagina, B.B. (1993) Relationships between structural parameters and chemical composition of micas. Clay Minerals, 28, 603–624.

Smyth, J.R., Jacobsen, S.D., Swope, R.J., Angel, R.J., Arlt, T., Domanik, K., and Holloway, J.R. (2000) Crystal structures and compressibilities of synthetic $2M_1$ and 3T phengite micas. European Journal of Mineralogy, 12, 955–963.

Sokolova, T.N., Drits, V.A., Sokolova, A.L., and Stepanov, S.S. (1976) Structural and mineralogical characteristics and conditions of formation of leucophyllite from salt-bearing deposits of Inder. Litology and Raw Materials, 6, 80–95 (in Russian).

Środoń, J. (1999) Nature of mixed-layer clays and mechanisms of their formation and alteration. Annual Reviews Earth and Planetary Science, 27, 19–53.

Środoń, J. and Eberl, D.D. (1984) Illite. In S.W. Bailey, Ed., Micas, 13, p. 495–544. Reviews in Mineralogy, Mineralogical Society of America, Chantilly, Virginia.

Środoń, J., Elssass, F., McHardy, W.J., and Morgan, D.J. (1992) Chemistry of illite-smectite inferred from TEM measurements of fundamental particles. Clays and Clay Minerals, 32, 337–349.

Takeda, H., Naga, N., and Sadanaga, R. (1971) Structural investigation of polymorphic transition between $2M_2$ – 1M lepidolite and $2M_1$-muscovite. Mineralogical Journal, 6, 203–215.

Viczián, I. (1997) Hungarian investigations on the "Zempleni" illite. Clays and Clay Minerals, 45, 114–115.

Wang, J., Toby, B.H., Lee, P.L., Ribaud, L., Antao, S., Kurtz, C., Ramanathan, M., Von Dreele, R.B., and Beno, M.A. (2008) A dedicated powder diffraction beamline at the Advanced Photon Source: Commissioning and early operation results. Review of Scientific Instruments, 79, 85–105.

Zviagina, B.B., Sakharov, B.A., and Drits, V.A. (2007) X-ray diffraction criteria for the identification of *trans*- and *cis*-vacant varieties of dioctahedral micas. Clays and Clay Minerals, 55, 467–480.